

Influence of the particle distribution on dust explosions in the 20 L sphere

Kasun Weerasekara^{a,b,*}, Stefan H. Spitzer^c, Sabine Zakel^a, Holger Grosshans^{a,b}

^aPhysikalisch-Technische Bundesanstalt, Bundesallee 100, Braunschweig, 38116, Germany

^bOtto von Guericke University of Magdeburg, Universitätsplatz 2, Magdeburg, 39106, Germany

^cEIJI-Tech, Universitätspark 1/1, Schwäbisch Gmünd, 73525, Germany

Abstract

It is essential to standardize the safety characteristics of dust explosions to mitigate their impact on the process industries. The 20 L sphere primarily investigates the safety characteristics, namely explosion pressure (P_{ex}) and the rate of pressure rise ($(dP/dt)_{\text{ex}}$), of dust explosions at the laboratory level. Ensuring uniform dust distribution inside the sphere is essential for accurate data acquisition and standardization. However, whirls created by the incoming flow through the nozzle yield particles to concentrate near the wall before ignition. This study simulated the explosion inside a 20 L sphere to investigate the impact of near-wall particle concentration on the safety characteristics. The OpenFOAM model based on the Euler-Lagrangian approach was benchmarked against experimental data of lycopodium dust explosions. A novel radial homogeneity parameter Φ ($0 \leq \Phi \leq 1$) quantifies the near-wall particle concentration. The parameter Φ is calculated using a power law based on the radial component of particle coordinates, $\Phi = 1$ indicating a uniform distribution, and $\Phi = 0$ for all particles concentrating on the wall. Different particle distributions ($\Phi = 0.1, 0.2, \dots, 1$) are initiated before ignition. As Φ decreases from 1, P_{ex} and $(dP/dt)_{\text{ex}}$ first decrease, but beyond a certain point, both parameters increase. At $\Phi = 0.1$, both P_{ex} and $(dP/dt)_{\text{ex}}$ reach their highest values, which are 1.75% and 10.1% higher than the uniform distribution, respectively. The lowest values arise at $\Phi = 0.7$, with reductions of 0.25% and 5.6% compared to the uniform distribution. Thus, high near-wall concentrations enhance explosion intensity, while moderate concentrations result in lower intensity than the uniform distribution.

Keywords:

Dust explosions, Safety characteristics, Near wall particle concentration, 20 L sphere, Numerical simulation, OpenFOAM

1. Introduction

Dust explosions in process industries are caused by the ignition of fine combustible particles suspended in air, as commonly seen in grain silos, flour mills, and coal mines. Between the years 1785 and 2012, over 2870 dust explosions occurred worldwide, killing more than 4800 people [1]. Therefore, understanding and regulating dust explosions is essential to protect human lives and physical resources.

A dust explosion occurs when an oxidant, combustible dust, dispersion of the dust, confinement, and an ignition source are all present. Eliminating one or more of these required elements can prevent the initiation of a dust explosion. To minimize the harm of these events, it is necessary to evaluate the safety characteristics of the explosion. In the laboratory, the 20 L sphere provides the explosion's pressure (P_{ex}), and pressure

rise $(dP/dt)_{\text{ex}}$, and the MIKE 3 apparatus the minimum ignition energy. This study focuses on the 20 L sphere.

The 20 L sphere contains two chemical igniters at its center, which ignite the explosive dust as it enters through a nozzle (Figure 1a). Two internal pressure sensors measure the pressure versus time (Figure 1b). The initial pressure inside the sphere remains at 0.4 bar, below atmospheric pressure, and the dust container is pressurized up to 21 bar. Once the valve opens, dust particles flow through the nozzle into the sphere at high pressure. Ignition begins after dust particles fully disperse within the sphere. A brief waiting period, the ignition delay typically of 60 ms, ensures uniform dust dispersion. When ignition starts, the dust cloud explodes, and the pressure rapidly increases to a peak value before gradually decreasing.

Accurately determining the dust's minimum explosible concentration (MEC) and other parameters requires

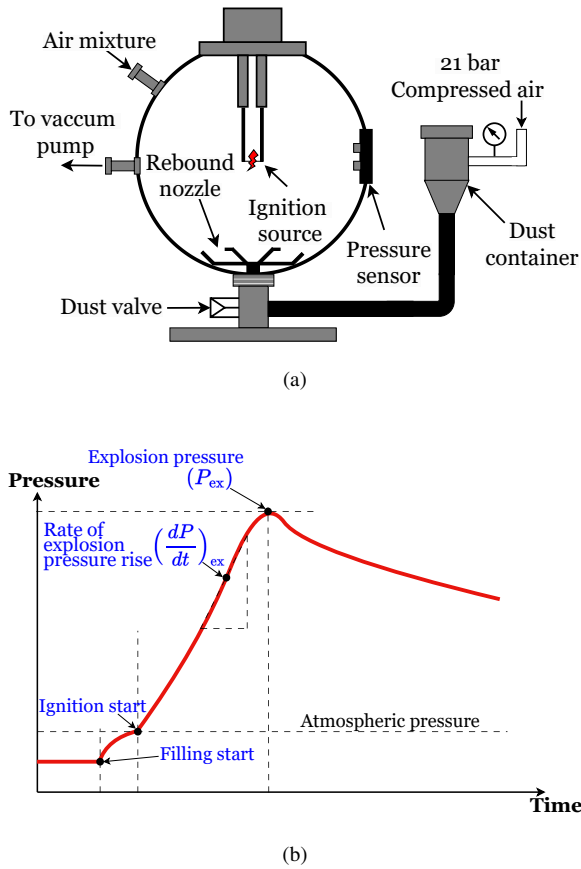


Figure 1: (a) Schematics of the 20 L sphere and (b) pressure evolution in the experiment.

a uniform particle distribution in the sphere [2]. To achieve a uniform distribution, selecting an appropriate nozzle is essential. However, the commonly used rebound nozzle does not produce a uniform dust distribution, and the particle concentration tends to be higher near the sphere walls.

Cashdollar K. L. et al. measured local variations in dust concentrations using optical probes at different locations inside the sphere [2]. A Siwek sphere with a setup of six optical probes, arranged in two sets of three probes and extending from the wall to the center along two perpendicular radial directions, revealed that dust particle concentrations were higher near the chamber walls than at the center [3]. Afterward, a transparent 20 L Siwek sphere enabled direct observation of the dust dispersion before ignition by shadowgraphy. Findings indicated a higher concentration of particles near the wall, especially around the rebound nozzle, suggesting that alternative nozzles could improve particle distribution homogeneity [4].

However, experimental setups have limitations in visualizing exact distributions inside the sphere. Well-validated 3D computational fluid dynamic (CFD) simulations of the 20L sphere can provide more details on the particles than experiments. For instance, a 3D CFD simulation using ANSYS-FLUENT showed that turbulent vortices caused higher dust concentrations near the vessel walls [5]. This occurs because particles first exit the nozzle and strike the wall, then move along the wall to the top of the sphere, falling and merging with the inflow from the nozzle. This movement induces two counter-rotating vortices inside the chamber. Eventually, the particles settle down, which reduces turbulence. Further CFD analysis using OpenFOAM evaluated particle distribution for a new nozzle design and revealed that while the rebound nozzle resulted in high particle concentrations near the wall, the new design improved the concentration in the middle compared with the previous nozzle and a more even distribution throughout the sphere [6].

In summary, experiments and simulations confirmed that particles in the sphere distributed inhomogeneously, with higher concentrations near the wall before the ignition. The present study investigated, through numerical simulations, how the particle concentration affects the safety characteristics. Section 2 details the computational model, and Section 3 presents the validation of the CFD model against experimental data. The analysis introduces a new parameter to evaluate the degree of homogeneity inside the chamber. Multiple simulations examine different levels of particle distribution, and Section 4 discusses the resulting explosion parameter changes and comparisons. Section 5 presents the study's conclusions and future directions.

2. Computational Methodology

This study applies numerical simulations along with experiments for benchmarking. This section discusses the computational methodology employed for the simulations. A dust explosion is a multiphysics and multiphase problem, including a fluid (air mixture) and a solid phase (dust particles). As a multiphase simulation technique, this study uses the Euler-Lagrangian approach, which couples the continuous phase in the Eulerian framework with the dispersed phase in the Lagrangian framework. This method is particularly effective for flows with a relatively low volume fraction of the dispersed phase, such as dust explosions.

To model the particle-fluid flow interactions and chemical reactions in dust explosions, we used the coalChemistryFoam solver of the OpenFOAM 2012

open-source package. This solver accounts for two-way coupling, i.e., the momentum transfer from the particles to the fluid and vice versa.

2.1. Gas Phase Governing Equations

The governing equations are based on Reynolds-Averaged Navier-Stokes (RANS) equations ((1) and (2)), along with the energy and species conservation equations ((4) and (3)),

$$\frac{\partial \rho}{\partial t} + \nabla \cdot (\rho \mathbf{u}) = S_M, \quad (1)$$

$$\frac{\partial(\rho \mathbf{u})}{\partial t} + \nabla \cdot (\rho \mathbf{u} \otimes \mathbf{u}) = -\nabla p + \nabla \cdot \boldsymbol{\tau} - \nabla \cdot (\rho \mathbf{R}_f) + \rho \mathbf{g} + S_F, \quad (2)$$

$$\begin{aligned} \frac{\partial(\rho h)}{\partial t} + \frac{\partial(\rho K)}{\partial t} + \nabla \cdot (\rho \mathbf{u} h) + \nabla \cdot (\rho \mathbf{u} K) - \nabla \cdot (\alpha_{\text{eff}} \nabla h) = \\ \frac{\partial p}{\partial t} + \rho \mathbf{u} \cdot \mathbf{g} + \dot{Q}_{\text{react}} + \dot{Q}_{\text{radi}} + S_E, \end{aligned} \quad (3)$$

$$\frac{\partial(\rho Y_k)}{\partial t} + \nabla \cdot (\rho \mathbf{u} Y_k) - \nabla \cdot (D_{\text{eff}} \nabla (\rho Y_k)) = \bar{\omega}_k + S_{Y_k}. \quad (4)$$

The perfect gas law, serving as the equation of state,

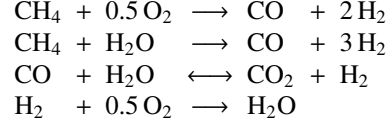
$$\rho = \frac{p}{(R_u/W)T} \quad (5)$$

closes the system of governing equations.

The source terms of the mass, momentum, energy, and species transport equations (S_M , S_F , S_E , and S_{Y_k}) couple the Lagrangian to the Eulerian equations. The source terms for the mass equation arise from moisture evaporation, devolatilization, and solid particle conversion. The source terms of the momentum equations link to the particles' drag. Ignition, radiative heating, and heat addition or absorption from chemical reactions form the source terms of the energy equation. In the species transport equation, reactants and products serve as source terms. The following chapters detail the modeling of these source terms.

2.1.1. Homogeneous Chemical Reaction Modeling

This section discusses the mathematical modeling of chemical reactions of the volatiles in the gas phase. This study adopts a four-step global mechanism to model the oxidation of CH_4 , initially developed for hydrocarbon combustion [7]. This model implements 4 Arrhenius reactions, with two irreversible reactions and two reversible reactions:



The kinetic rates for each reaction are provided by Islas et al. [8].

As an example, the reaction modeling is explained for a one-step methane combustion mechanism ($\text{CH}_4 + 2\text{O}_2 \rightarrow \text{CO}_2 + 2\text{H}_2\text{O}$). This mechanism is considered an 'Irreversible Arrhenius Reaction,' a temperature-based reaction rate. For methane combustion,

$$k_f = AT^\beta \exp(-T_a/T) \quad (6)$$

calculates the reaction rate constant with $A = 7 \times 10^6 \text{ mol m}^{-3} \text{ s}^{-1}$, $\beta = 0$, and $T_a = 10\,063 \text{ K}$ [9].

Generally,

$$\sum_{k=1}^K v'_{k,i} \mathcal{X}_k \rightleftharpoons \sum_{k=1}^K v''_{k,i} \mathcal{X}_k \quad i = 1, 2, \dots, I \quad (7)$$

expresses the set of I reactions with K species. Here, $v'_{k,i}$, $v''_{k,i}$, and \mathcal{X}_k are the forward and backward stoichiometric coefficients and the chemical symbol of the species k , respectively. They become for methane combustion, $I = 1$, $v'_{k,i} = [1 \ 2 \ 0 \ 0]$, $v''_{k,i} = [0 \ 0 \ 1 \ 2]$, and $\mathcal{X}_k = [\text{CH}_4 \ \text{O}_2 \ \text{CO}_2 \ \text{H}_2\text{O}]^T$.

The chemical reaction rate ($\dot{\omega}$) describes the velocity of a chemical reaction. It represents the change in the concentration of species for the i^{th} reaction, expressed as,

$$\dot{\omega}_i = k_{f,i} \prod_k [\mathcal{X}_k]^{v'_{k,i}} - k_{r,i} \prod_k [\mathcal{X}_k]^{v''_{k,i}}, \quad (8)$$

where $k_{f,i}$, $k_{r,i}$, and $[\mathcal{X}_k]$ are the forward and backward kinetic rates and the concentration of specie k , respectively. Methane combustion has no backward reaction ($k_{r,i} = 0$). Thus,

$$\dot{\omega}_1 = k_{f,i=1} [\text{CH}_4]^1 [\text{O}_2]^2. \quad (9)$$

The reaction rate of species k , which the species conservation equation (4) requires, is [10]

$$\dot{\omega}_k = \sum_i \dot{\omega}_i (v'_{k,i} - v''_{k,i}). \quad (10)$$

Hence, for methane combustion, the reaction rates for each species are

$$\begin{bmatrix} \dot{\omega}_{\text{CH}_4} \\ \dot{\omega}_{\text{O}_2} \\ \dot{\omega}_{\text{CO}_2} \\ \dot{\omega}_{\text{H}_2\text{O}} \end{bmatrix} = \begin{bmatrix} \dot{\omega}_1(1-0) \\ \dot{\omega}_1(2-0) \\ \dot{\omega}_1(0-1) \\ \dot{\omega}_1(0-2) \end{bmatrix} = \begin{bmatrix} \dot{\omega}_1 \\ 2\dot{\omega}_1 \\ -\dot{\omega}_1 \\ -2\dot{\omega}_1 \end{bmatrix}. \quad (11)$$

As an inter-specie, N_2 does not participate in chemical reactions. Consequently,

$$Y_{N_2} = 1 - \sum_{k \neq N_2} Y_k \quad (12)$$

calculates the mass fraction for N_2 explicitly.

2.1.2. Turbulence-Chemistry Interaction Model

Combustion involves complex interactions between fluid dynamics and chemistry, with turbulence playing a key role by enhancing reactant mixing and accelerating reactions. To model the chemical reaction rates for each species in Equation (4), the Partially Stirred Reactor (PaSR) model calculates the reaction rate using the turbulent, τ_t , and chemical, τ_c , time scales, along with the instantaneous reaction rate as follows [11],

$$\bar{\omega}_k = \frac{\tau_c}{\tau_c + \tau_t} \omega_k. \quad (13)$$

The turbulent time scale is calculated as a fraction of the turbulence integral time scale ($\tau_{t,I}$),

$$\tau_t = C_m \tau_{t,I} = C_m \sqrt{\frac{\nu_{\text{eff}}}{\varepsilon}}, \quad (14)$$

where C_m is the mixing coefficient, ν_{eff} the effective kinematic viscosity, and ε the turbulent dissipation rate. As an estimation, the turbulence time scale equals the root mean of integral and Kolmogorov time scales ($\tau_{t,K}$) [11] given as,

$$\tau_t \approx \sqrt{\tau_{t,I} \tau_{t,K}} = \sqrt{\frac{k}{\varepsilon} \left(\frac{\nu}{\varepsilon}\right)^{1/2}}. \quad (15)$$

From the Equations 14 and 15, the mixing coefficient is computed by,

$$C_m = \sqrt{\frac{1}{1 + C_\mu Re_t}}, \quad (16)$$

where $C_\mu = \mu_t \varepsilon / (\rho k)$ and $Re_t = k^2 / (\varepsilon \nu)$. C_m equals unity for laminar ($Re_t = 0$) and zero for highly turbulent flows ($Re_t \rightarrow \infty$). Typically, C_m is between 0.01 and 0.3 for turbulence flows; for example, $C_m \approx 0.1$ for $Re_t \approx 1000$.

The chemical time scale is the ratio of the total concentration to the production rate of the product species expressed as,

$$\tau_c = \sum_{i=1}^I \frac{c_{\text{total}}}{\sum_{k=1}^{K_{\text{products}}} \nu_{k,i} \cdot \omega_{k,i}}, \quad (17)$$

where c_{total} denotes the overall concentration of all species and K_{products} all product species.

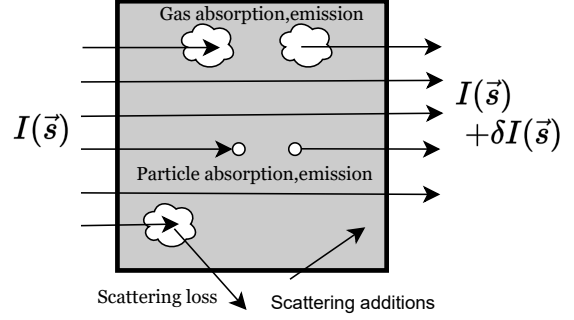


Figure 2: Overview of radiative transfer equation modeling inside a control volume.

2.1.3. Radiation Modeling

Due to the high temperature, radiation cannot be neglected and is a main heat source for particles from the fluid field before the flame-front arrives [12]. We solve the radiative transfer equation that describes the change in radiation intensity $I(\vec{s})$ in the direction of \vec{s} . The conservation of I includes emission and absorption according to the Stefan–Boltzmann law, scattering losses, and absorption by the gas (CO_2 and H_2O) and particles; see Figure 2 for an overview.

This study applies the discrete ordinates radiation model [13] because it accounts for gas participation in the radiative transfer equation. The discrete ordinates radiation model discretizes the angular space into a finite set of solid angles, each representing a direction, \vec{s} , and solves the radiative transfer equation for these angles.

2.2. Solid Phase Governing Equations

The governing equations for the dispersed solid phase are based on the Lagrangian particle tracking approach. Similar to the gas phase, the solid phase equations also consist of the conservation laws for mass, momentum, and energy,

$$\frac{dm_p}{dt} = \frac{dm_{\text{evp}}}{dt} + \sum \frac{dm_{\text{devol},k}}{dt} + \frac{dm_{\text{char}}}{dt}, \quad (18)$$

$$m_p \frac{d\mathbf{u}_p}{dt} = \mathbf{F}_d + \mathbf{F}_g, \quad (19)$$

$$m_p C_p \frac{dT_p}{dt} = \dot{q}_{\text{conv}} + \dot{q}_{\text{radi}} + \frac{1}{dt} \{ \Delta H_{\text{evp}} + \Delta H_{\text{devol}} + \Delta H_{\text{char}} \}. \quad (20)$$

According to mass conservation (Equation (18)), the combustion of a particle occurs in three main steps. As illustrated in Figure 3, an initial particle (such as

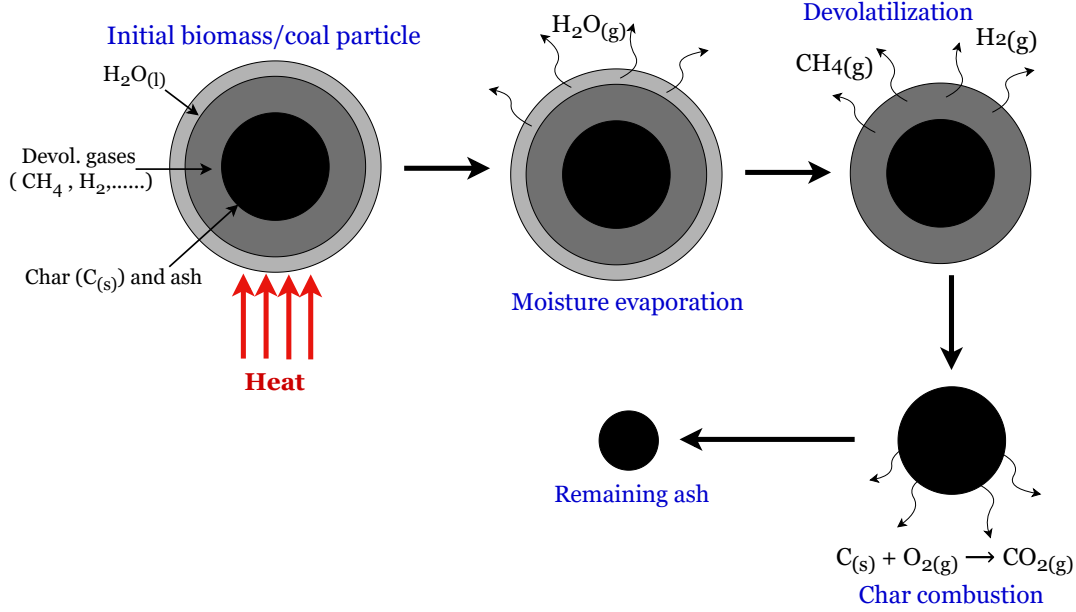


Figure 3: Overview of the biomass/coal particle combustion process.

biomass or coal) consists of char, moisture, and volatile gases. Upon particle heating, moisture evaporates first, followed by the release of volatile gases and, finally, char combustion. These products are the source terms for each species' continuity equation. In the momentum equation (Equation (19)), drag and buoyancy are the external forces on the particle. The energy balance (Equation (20)) for the particles involves convection, radiation, and latent heat.

2.2.1. Moisture Evaporation Model

We assume water to be the only liquid in the particles. The Water vapor mass transfer rate by evaporation reads,

$$\frac{dm_{\text{evp}}}{dt} = A_p Ni W_{\text{H}_2\text{O}}, \quad (21)$$

where, A_p is the particle's surface area and Ni is the molar flux of water vapor,

$$Ni = k_c(C_s - C_\infty). \quad (22)$$

The vapor concentration at the surface,

$$C_s = \frac{p_{\text{sat}}}{RT_s}, \quad (23)$$

is based on the saturation pressure (p_{sat}) of the water vapor at fluid film temperature (T_s), which is calculated

using the rule of thirds for particle and fluid temperatures at the particle surface,

$$T_s = \frac{2T_p + T_f}{3}. \quad (24)$$

The water vapor concentration in the bulk gas, C_∞ , for a vapor molar fraction of $X_{\text{H}_2\text{O}}$ is

$$C_\infty = X_{\text{H}_2\text{O}} \frac{p}{RT_s}. \quad (25)$$

The mass transfer coefficient reads

$$k_c = \frac{Sh}{d_p} D_{\text{H}_2\text{O}}, \quad (26)$$

where d_p is the particle diameter, $D_{\text{H}_2\text{O}}$ the vapor diffusivity, and Sh the Sherwood number. The Sherwood Number (Sh), analogous to the Nusselt number in heat transfer, represents the ratio between the total (convective and diffusive) to diffusive mass transfer. According to dimensional analysis, Sh is a function of the Reynolds and the Schmidt ($Sc = \nu/D_{\text{H}_2\text{O}}$) numbers. We estimate this function by the Ranz-Marshall correlation [14],

$$Sh = 2 + 0.6 Re_p^{1/2} Sc^{1/3}. \quad (27)$$

The particle Reynolds number is given by,

$$Re_p = \frac{\rho_f d_p |\mathbf{u}_f - \mathbf{u}_p|}{\mu_f}. \quad (28)$$

The required heat for moisture evaporation (ΔH_{evp}) is calculated from the enthalpy difference between the gas phase and the water vapor at the given pressure and temperature.

2.2.2. Devolatilization Model

Devolatilization decomposes volatile matter (gas) from a particle until the remaining char combusts. Thermogravimetric analysis and derivative thermogravimetry determine experimentally T_{devol} , the temperature at which the devolatilization starts, and ΔH_{devol} , the required latent energy [15]. In this simulation, a first-order kinetic rate model calculates the devolatilized mass of species,

$$\frac{dm_{\text{devol},k}}{dt} = k(T)(m_{\text{devol},k} - m_{\text{devol},k,0}), \quad (29)$$

where $dm_{\text{devol},k}$ is the devolatilized mass, $m_{\text{devol},k}$ is the current mass, and $m_{\text{devol},k,0}$ is the initial mass of species k . The kinetic rate $k(T)$ is temperature-dependent and is determined by an Arrhenius equation.

2.2.3. Surface Reaction Model (Char Combustion)

After the complete devolatilization, the particle remains as char, which we assume to consist of pure carbon. Then, this char undergoes oxidation,



Therein, the stoichiometric coefficient $S b$ is set to unity.

Mass consumption of char is, according to the kinetic-diffusion limited rate model [16],

$$\frac{dm_{\text{char}}}{dt} = -A_p p_{O_2} \frac{DK}{D + K}, \quad (31)$$

where the partial pressure of O_2 is

$$p_{O_2} = \rho R T_f \left(\frac{Y_{O_2}}{W_{O_2}} \right), \quad (32)$$

the diffusion rate coefficient,

$$\mathcal{D} = C_1 \frac{(T_f + T_p)^{0.75}}{2d_p}, \quad (33)$$

and the kinetic rate coefficient,

$$\mathcal{K} = C_2 \exp(-E_a/RT_p). \quad (34)$$

In these equations, C_1 , C_2 , and E_a are the mass diffusion-limited rate constant, the kinetics-limited rate pre-exponential constant, and the kinetics-limited rate activation energy, respectively.

Due to the reaction, it is needed to determine the consumption of O_2 and the production of CO_2 and update the gas-phase equations using the molar consumption,

$$\Omega = \frac{dm_{\text{char}}}{W_c}. \quad (35)$$

Hence, the consumption of O_2 equals

$$dm_{O_2} = \Omega S b W_{O_2}, \quad (36)$$

and the production of CO_2 is

$$dm_{CO_2} = \Omega(W_c + S b W_{O_2}). \quad (37)$$

The energy released from char combustion is given by,

$$\Delta H_{\text{char}} = h_{\text{ret}} \Delta h_{f,CO_2} dm_{CO_2}, \quad (38)$$

where $\Delta h_{f,CO_2}$ is the formation enthalpy of CO_2 . However, a portion of this total released energy is transferred to the particle itself, apart from the gas phase. This portion is defined by the retention coefficient h_{ret} , which is assumed to be 0.3 for char conversion to CO_2 [17].

2.2.4. Forces Acting on Solid Particles

The drag force is given by the expression

$$\mathbf{F}_d = C_d A \frac{\rho_f}{2} |\mathbf{u}_f - \mathbf{u}_p| (\mathbf{u}_f - \mathbf{u}_p), \quad (39)$$

where A is the cross-section area of the particle, and the drag coefficient is calculated by the empirical correlation [18, 19],

$$C_d = \begin{cases} \frac{24}{Re_p} \left(1 + \frac{1}{6} Re_p^{2/3} \right) & Re_p \leq 1000 \\ 0.424 & Re_p > 1000. \end{cases} \quad (40)$$

The combined buoyancy and gravitational force reads

$$\mathbf{F}_g = m_p \left(1 - \frac{\rho_f}{\rho_p} \right) \mathbf{g}. \quad (41)$$

2.2.5. Heat Transfer Model

This section describes the models for the source terms in the energy conservation equation of the particles (20). The convective heat transfer between the fluid and a particle is

$$\dot{q}_{\text{conv}} = h A_p (T_f - T_p). \quad (42)$$

The convective heat transfer coefficient, h , is according to the Nusselt number definition,

$$h = \frac{k_f}{d_p} Nu, \quad (43)$$

where k_f is the thermal conductivity of the fluid. The Nusselt number, Nu , is a function of the Reynolds and Prandtl, Pr , numbers. Analogous to Equation (27), the Nusselt number follows the Ranz-Marshall correlation as [14]

$$Nu = 2 + 0.6Re_p^{1/2}Pr^{1/3}. \quad (44)$$

from the empirical and the particle Reynolds number.

Due to moisture evaporation from the surface, the convective heat transfer is corrected by the ‘Bird Correction’ [20],

$$\dot{q}_{\text{conv,corrected}} = h \frac{\beta}{e^\beta - 1} A_p (T_f - T_p), \quad (45)$$

where, β is $NiC_{p,H_2O}W_{H_2O}$ (cf. Equation (22)).

Particles participate in both the absorption and emission of radiation energy. Therefore, the resultant radiative heat transfer,

$$\dot{q}_{\text{radi}} = \dot{q}_{\text{radi,absorption}} - \dot{q}_{\text{radi,emission}} = A_p \epsilon_p \left[\frac{G}{4} - \sigma T_p^4 \right]. \quad (46)$$

The radiation model calculates the incident radiation, G , for each fluid cell by solving the radiative transfer equation, where ϵ_p is the particle emissivity and σ denotes the Stefan–Boltzmann constant.

The energy equation includes three parts of heat transfer from the combustion processes. The enthalpy difference from the moisture evaporation model determines ΔH_{evap} . Thermogravimetry experiments determine the value of ΔH_{devol} . The latent heat from char combustion, ΔH_{char} , is calculated from the formation enthalpy of CO_2 and the mass of CO_2 generated from char combustion. Moisture evaporation and devolatilization absorb energy from the fluid (endothermic process), and char combustion releases heat into the fluid (exothermic process).

2.3. Coupling between Gas and Particle Phases

This section describes the link between source terms in the gas-phase governing equations (1) to (4) and the particle-phase governing equations (18) to (20).

The rate of a species transferred from the particles P within a volume dV to the gas equals the source term in the gas-phase species transport equation,

$$S_{Y,k} = \frac{d}{dV} \sum_i^P \frac{dm_{i,k}}{dt}, \quad (47)$$

and accordingly, the source term in the gas-phase continuity equation becomes

$$S_\rho = \sum_k S_{Y,k}. \quad (48)$$

The sums of the drag and buoyancy forces of the particles inside a volume equal the source terms for the gas phase momentum equation. Analogously, the sum of the particles’ net heat transfer of the three combustion processes is the source term of the gas phase energy equation.

3. Set-up, Comparison to Experiments, and Mesh Convergence

We validate the numerical solver by comparing it to experimental results of lycopodium dust explosions in the 20 L sphere. For the experiments, we apply the setup documented by [21], who explored the distribution of lycopodium dust inside the sphere for various nozzle types. As mentioned in the Introduction, normally, the dust is stored in a small canister and released into the 20 L sphere via a valve. However, we used the ‘Janovsky’ nozzle in the experiments and placed the dust directly in the sphere, which resulted in a more uniform distribution within the sphere. Further, this approach ensures the total dust mass within the sphere, contrary to rebound or annular nozzles, where some dust can remain trapped within the nozzle and connecting pipes. In other words, we chose an experimental setup and procedure optimized for model validation.

3.1. Chemical and Material Properties of Lycopodium

This section documents the chemical and material properties of lycopodium dust and the numerical input for the simulation. Explosion parameters vary with the precise source of the dust, even if the material is nominally the same. The composition and size distributions can differ for each dust. Additionally, some property trade-offs reduce simulation complexity.

Explosive dust contains solid material, moisture, and volatile gases. Volatile gases may include CH_4 , H_2 , CO , and others. In this study, we assume that the volatile gas is CH_4 and the solid of the particle is pure carbon (C) [22]. A Sartorius MA35 test determined the moisture content twice, yielding values of 3.4 weight-% and 3.8 weight-%, which suggests the presence of volatile matter [21].

One reason why we decided to study lycopodium is that its particles have a narrow size distribution. A Malvern Mastersizer3000 measured a mean particle size of $d_{50} = 30.6 \mu\text{m}$, $d_{10} = 25.3 \mu\text{m}$, and $d_{90} = 36.9 \mu\text{m}$. In the simulation, all particles are spherical with a uniform diameter of d_{50} . The material density of lycopodium dust is 100 kg/m^3 , and the specific heat capacity is $C_p = 1005 \text{ J/kgK}$. The devolatilization temperature

is $T_{\text{dev}} = 483$ K, and the devolatilization latent heat is $\Delta H_{\text{dev}} = 3.07 \times 10^5$ J/kg [23].

3.2. Numerical Set-up

This section provides key numerical inputs for the simulations.

The geometry is a sphere with a radius of 0.168 m, equivalent to a volume of 20 L. For simplicity, the nozzle, ignition source components inside the sphere, and the dust-filling mechanism are not considered for modeling. Instead, the dust particles are initially placed within the sphere.

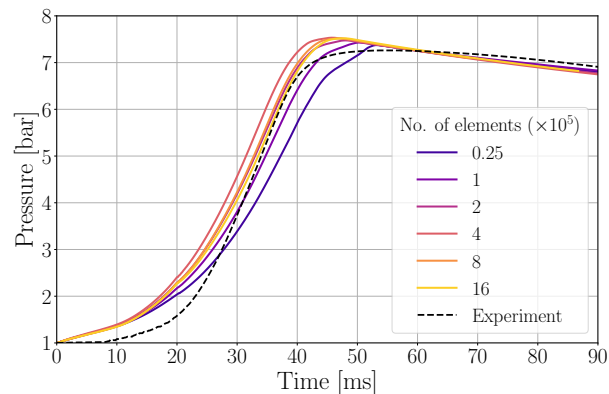
The simulation domain has a single boundary, the wall of the sphere. The wall temperature is maintained at a fixed value of 294 K, corresponding to the water jacket in the experiment. The velocity boundary condition is no-slip, and the pressure is specified as a zero gradient at the wall. Standard wall functions are used for the turbulence parameters (k , ε , and ν_t). As initial values, the temperature, pressure, and velocity field are set uniformly to 294 K, 1 bar, and zero, respectively.

Ignition is modeled by adding a temperature patch inside the domain. The ignition parameters are finalized using an iterative approach adopted from Pan [24]. Accordingly, the ignition volume consists of two spheres, each with a radius of 4 cm, positioned at the center of the sphere with a center-to-center distance of 8 cm. The temperature of the ignition source is time-dependent, following a first-order polynomial ($T = 2 \times 10^5 t$ K/s + 294 K), with an ignition duration of $t = 20$ ms as an average value of typical ignition time between 10-30 ms.

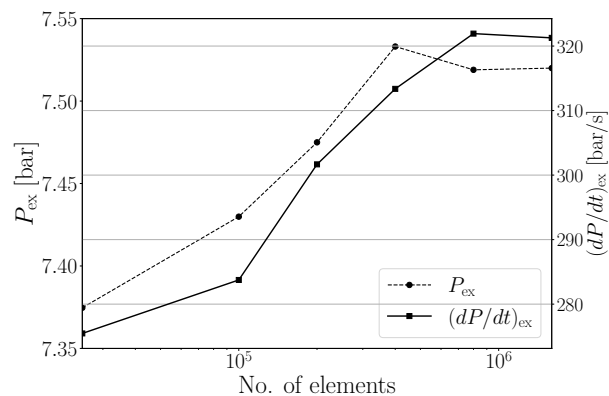
The CFL number is set to 0.1, and a first-order Euler time integration scheme is used. The spatial discretization schemes are second-order accurate. The $k-\varepsilon$ turbulence model, commonly used in combustion problems, is selected. The chemical solver uses an implicit Euler method to handle the small time steps. Additionally, a relaxation factor of 0.8 is applied to all fields for simulation stability.

3.3. Mesh Convergence

The mesh of the spherical domain consists of 7 blocks, with 1 cubical block at the center and 6 spherical caps surrounding it. All elements are hexagonal, and the mesh is structured. The experiment provides the time-resolved pressure for benchmarking the CFD model. For the mesh convergence test, we computed the dust explosion on 6 meshes with element counts ranging from 0.25×10^5 to 16×10^5 . Figure 4a compares the pressure developments per mesh to the experimental result. Figure 4b presents of P_{ex} and $(dP/dt)_{\text{ex}}$ against



(a)



(b)

Figure 4: (a) Pressure curves of simulations with different mesh sizes compared to experimental data. (b) P_{ex} and $(dP/dt)_{\text{ex}}$ for different mesh sizes.

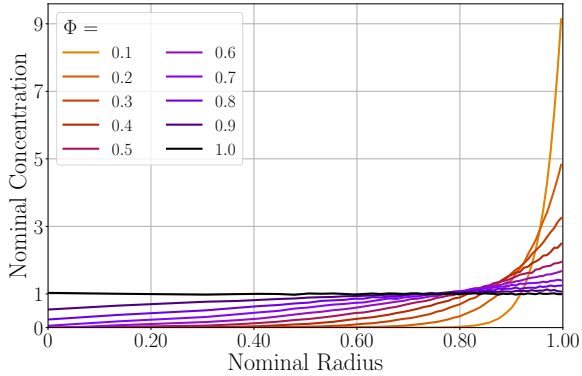
the mesh size. Evaluating the computational time and accuracy, we decided to use the mesh with 8×10^5 elements, having errors of 3.5% and 2.5% relative to the experimental data for P_{ex} and $(dP/dt)_{\text{ex}}$. Further, we use 5×10^5 particles.

4. Particle Homogeneity Analysis and Results

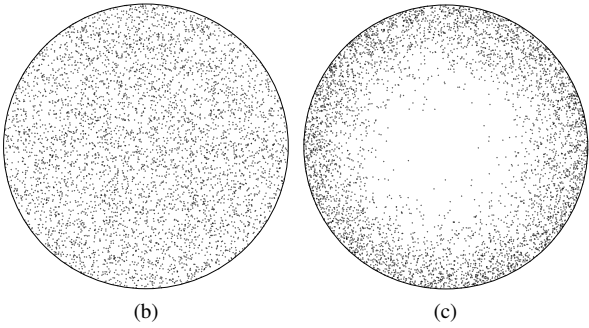
4.1. Initial Particle Distribution

Lycopodium dust achieves a comparatively uniform distribution before ignition, which is why it was selected for the benchmark as a model dust. Nevertheless, as discussed in the introduction, particles are generally more concentrated toward the wall region than uniformly distributed. Therefore, this study investigates how the particle distribution affects the safety characteristics.

To this end, we start the simulations using different initial particle distributions, where the coefficient Φ



(a)



(b)

(c)

Figure 5: Initial particle distribution (a) along the radial coordinate, for (b) $\Phi = 1$, and (c) $\Phi = 0.5$.

characterizes each distribution's the radial homogeneity. First, we generate a uniform distribution of particles in a unit sphere, each particle having a distance to the unit sphere's center of r_{uni} . Then, we scale the radial distance of the particles to the sphere's center by $r_{\Phi} = Rr_{\text{uni}}^{\Phi}$, where $R = 0.168$ m is the sphere's radius. Thus, Φ varies between 0 and 1, where $\Phi = 0$ implies that all particles are placed at the wall and $\Phi = 1$ that the particles are uniformly distributed.

Multiple simulations explored the effect of particle radial distribution on explosions by varying the particle distributions by $\Phi = 0.1, 0.2, 0.3, \dots, 1$ while keeping all other parameters constant. Figure 5a shows the initial nominal concentration (relative to the uniform distribution concentration) of the particles along the radial coordinate normalized by the sphere's radius. For the $\Phi = 1$ (Figure 5b), the concentration is uniform along the radius. For $\Phi = 0.5$ (Figure 5c), the particles concentrate at the wall. For the $\Phi = 0.1$, most particles consolidate in the outer 20% of the radius, with a concentration 9 times higher near the wall than the uniform distribution.

4.2. Safety characteristics

Figure 6 shows the pressure and pressure gradient development curves for each particle distribution. When Φ decreases from 1 to 0.4, it takes longer to reach the explosion pressure. For a further decrease below $\Phi = 0.4$, the trend reverses, and the explosion pressure is reached faster. When particles are uniformly distributed and ignition starts, the ignition kernel covers some particles, initiating an explosion. Consequently, the flame front propagates rapidly, driven by the chain reactions of volatile gas combustion; the pressure and the rate of pressure rise increase.

In contrast, a void exists at the center (near the igniter) when particles are closer to the walls. Upon ignition, the flame front takes more time to reach and ignite the particles, thus delaying the explosion. When particles are concentrated near the wall ($1 > \Phi > 0.4$), the flame front propagates quickly toward the wall without significant combustion occurring in the midsection. This reduces the overall explosion intensity. However, if the particles are excessively concentrated near the wall ($\Phi < 0.4$), the flame front encounters a much higher particle concentration in that region, leading to an increased explosion rate, see Figure (6b).

Figure 6b shows the pressure gradient variation with time, indicating the explosion's intensity. Initially, higher Φ yield a rapid explosion rate, with the time to reach $(dP/dt)_{\text{ex}}$ being the shortest for the uniform distribution. Afterward, the time to reach $(dP/dt)_{\text{ex}}$ increases with Φ . However, due to the higher explosion rate near the wall, the time decreases again for $\Phi = 0.1$ and 0.2 . The lowest $(dP/dt)_{\text{ex}}$ occurs when $\Phi = 0.7$, while the highest occurs when $\Phi = 0.1$. The non-linear relationship between $\Phi = 0.1$ and $(dP/dt)_{\text{ex}}$ results from the competition between the reduced number of particles encountered by the flame front for low Φ while propagating through the sphere, which reduces $(dP/dt)_{\text{ex}}$, and encountering a higher particle concentration close to the wall, which increases $(dP/dt)_{\text{ex}}$.

Figure 7 visualizes the pressure and pressure gradient, normalized by their maximum value for each simulation. As suggested by [25], this provides an understanding of the explosion parameters independent of time. Nearly all distributions reach their $(dP/dt)_{\text{ex}}$ when the pressure approaches approximately 72% of its P_{ex} . Upon reaching $(dP/dt)_{\text{ex}}$, all distributions behave similarly: P_{ex} , $(dP/dt)_{\text{ex}}$ becomes negative, suggesting that the explosion completes, with the rate of pressure decrease being nearly equal for all distributions.

Figure 8 compares the explosion parameters to the uniform distribution, which means P_{ex} and $(dP/dt)_{\text{ex}}$ as

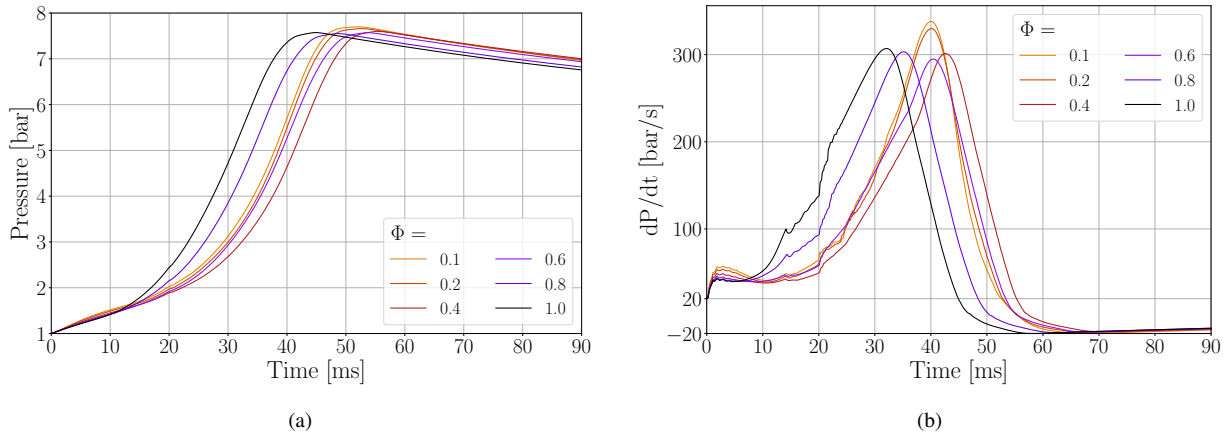


Figure 6: (a) Pressure and (b) pressure gradient in the sphere vs. time for different particle distributions.

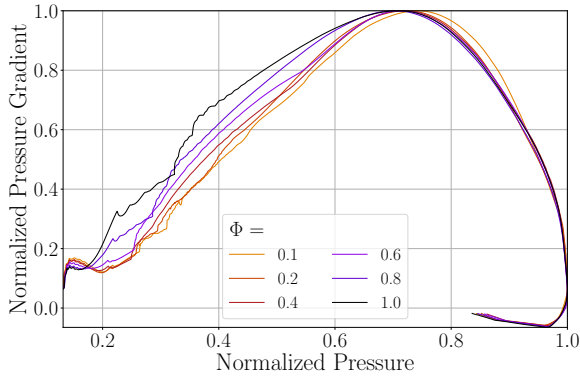


Figure 7: Normalized pressure gradient ($\frac{dP/dt}{(dP/dt)_{ex}}$) vs normalized pressure (P/P_{ex}).

percentages relative to $\phi = 1$. As ϕ decreases, both P_{ex} and $(dP/dt)_{ex}$ decrease and then increase beyond a certain point. Finally, for $\Phi = 0.1$, P_{ex} and $(dP/dt)_{ex}$ exceed the uniform distribution by 1.75% and 10%, respectively. The minimum P_{ex} occurs for $\phi = 0.8$, and $(dP/dt)_{ex}$ reaches its minimum for $\phi = 0.7$. This observation implies that moderate particle concentration near the wall ($\Phi = 0.7$) causes a less severe explosion than a uniform distribution.

4.3. Heat Dissipation Through the Wall

In the experiment, a water jacket is maintained around the sphere at a constant temperature of 294 K to prevent the wall from overheating. Similarly, the wall temperature is set to a constant value in simulations, as described in the boundary condition section.

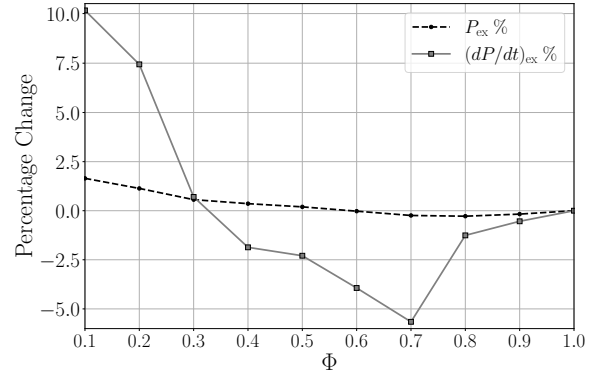
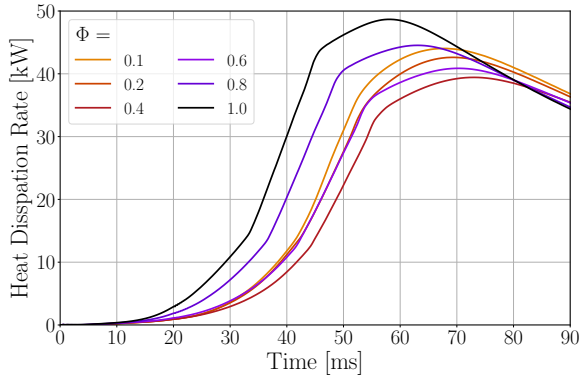


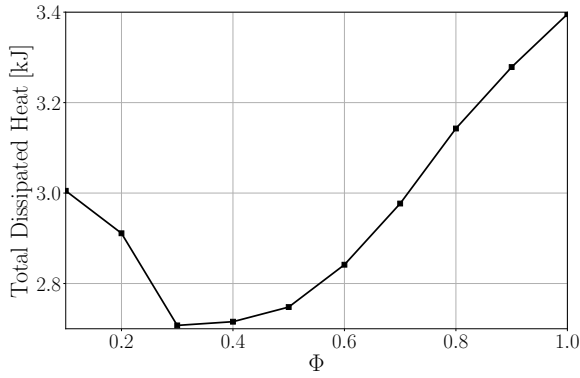
Figure 8: Percentage of variation of P_{ex} and $(dP/dt)_{ex}$ compared to uniform distribution for each Φ value.

Consequently, the energy released from explosions inside the sphere dissipates through the wall. According to the first law of thermodynamics, the total energy released by the dust combustion and ignition equals the gas' internal energy rise, which is proportional to the pressure rise, and the heat loss through the wall. Thus, a thermally well-insulated sphere, respectively adiabatic boundary conditions in the simulation, would result in a higher P_{ex} .

We calculated the heat loss through the wall by integrating the total heat flux, conductive and radiative, over the wall's surface area. Figure 9a shows the heat dissipation rate through the wall for each distribution. Since the temperature gradient drives the heat loss at the wall, it has a trend similar to the pressure development in Figure 6a. Figure 9b shows the total heat dissipation during the complete explosion for each distribution.



(a)



(b)

Figure 9: (a) Heat dissipation rate through the wall over time and (b) total dissipated heat through the wall

When particles distribute uniformly, they start combusting as soon as ignition starts. Therefore, the internal temperature and the heat flux through the wall increase. However, high particle concentration on the wall delays the combustion. Unburnt particles in the preheat zone absorb the combustion heat, reducing heat loss through the wall. Nevertheless, further increasing the near-wall concentration enhances energy dissipation through the wall. By balancing all of these factors, the lowest energy dissipation rate and total heat loss through the wall occurs for $\Phi = 0.3$.

4.4. Combustion Products

After moisture evaporation and devolatilization, the solid carbon mass undergoes oxidation. Figure 10 illustrates the percentage of particles remaining inside the sphere over time as a percentage of the initial number of particles. For a uniform distribution, all particles remain while Φ decreases, and the rate at which particles

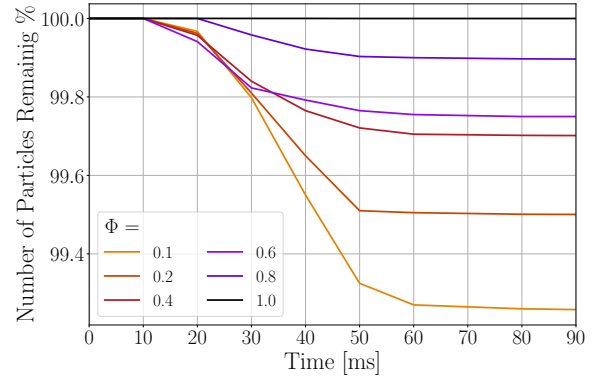


Figure 10: Percentage of remaining particles.

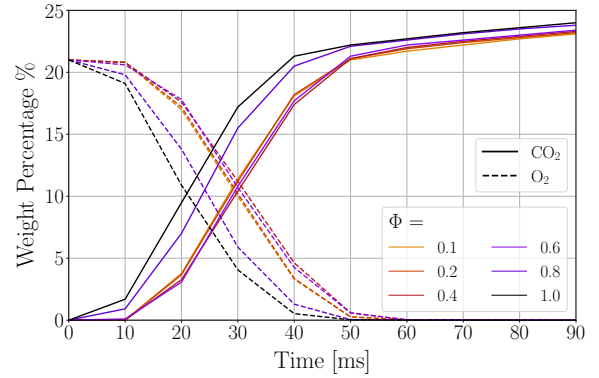


Figure 11: Weight of CO_2 and O_2 percentage variation

vanish increases. This could be due to the explosion of particles experiencing a high combustion rate near the sphere's surface.

Initially, the air-filled sphere contains only O_2 and N_2 , with molar fractions of 0.21 and 0.78, respectively. Since N_2 is an inert species, it does not participate in reactions. Ultimate end products after all multi-step reactions are CO_2 and H_2O . Production of CO_2 and consumption of O_2 indicate the amount of fuel or particles burned. Figure 11 shows some distributions' concentration variations of CO_2 and O_2 . After 60 ms, the entire O_2 is consumed for all distributions. However, CO_2 production continues in intermediate reaction steps. For the uniform distribution, the rate at which O_2 is consumed, and the production rate of CO_2 are lower compared to the distribution where particles are near the wall. The findings highlight the significant influence of particle distribution on combustion dynamics, particularly demonstrating how particle positioning within the sphere affects the rates of O_2 consumption and CO_2 production.

5. Conclusion

This study investigated the influence of particle distribution on the safety characteristics using a 20 L sphere. The results indicate that explosions are more intense when particles accumulate near the chamber walls than a uniform particle distribution despite a delay in the initial explosion. For the most non-uniform distribution studied ($\Phi = 0.1$), the maximum explosion pressure (P_{ex}) and the maximum rate of pressure rise ($(dP/dt)_{ex}$) reached their highest values, with increases of 1.75% and 10.1%, respectively, compared to the uniform distribution. Conversely, the lowest values for P_{ex} and $(dP/dt)_{ex}$ were observed at $\Phi = 0.7$, showing reductions of 0.25% and 5.6%, respectively, relative to the uniform distribution. These findings suggest that locally high particle concentrations enhance explosion intensity, whereas moderate concentrations result in lower intensities than a uniform distribution. The observations of heat loss rates and species concentrations further support this behavior.

This study could be extended to other volumes like the standard cubic meter sphere or other geometries, such as cylindrical chambers that model silos, and dust conveying pipes, to explore further strategies for minimizing explosion damage in process industries.

CRedit authorship contribution statement

K. Weerasekara: Writing – review & editing, Writing – original draft, Visualization, Software, Methodology, Conceptualization. S. H. Spitzer: Writing – review & editing, Software. S. Zakeel: Writing – review & editing, Supervision. H. Grosshans: Writing – review & editing, Supervision, Software, Funding acquisition.

Acknowledgments

This project has received funding from the European Research Council (ERC) under the European Union’s Horizon 2020 research and innovation program (Grant Agreement No. 947606 PowFEct).

Data availability

Data will be made available on request.

Appendix A. Nomenclature

Variables		
ρ	Density	[kg/m ³]
\mathbf{u}	Velocity	[m/s]
p	Pressure	[Pa]
t	Time	[s]
T	Temperature	[K]
\mathbf{g}	Gravitational acceleration	[m/s ²]
τ	Shear stress tensor	[N/m ²]
\mathbf{R}_f	Reynolds stress tensor	[N/m ²]
h	Specific enthalpy	[J/kg]
K	Specific kinematic energy	[J/kg]
α	Thermal conductive coefficient	[W/(mK)]
Q	Heat transfer rate	[W]
Y	Mass fraction	[-]
D	Mass diffusive coefficient	[m ² /s]
Re	Reynolds number	[-]
R_u	Universal gas constant	[J/(molK)]
W	Molar mass	[kg/mol]
ω	Chemical reaction rate	[mol/(m ³ s)]

Subscripts

f	Fluid
p	Particle
k	Species
t	Turbulent
eff	Effective (material+turbulent)
conv	Convection
react	Reaction
radi	Radiation

References

- [1] Z. Yuan, N. Khakzad, F. Khan, P. Amyotte, Dust explosions: A threat to the process industries, *Process Safety and Environmental Protection* 98 (2015) 57–71.
- [2] K. L. Cashdollar, K. Chatrathi, Minimum explosible dust concentrations measured in 20 L and 1-m³ chambers, *Combustion Science and Technology* 87 (1-6) (1993) 157–171.
- [3] O. Kalejaiye, P. R. Amyotte, M. J. Pegg, K. L. Cashdollar, Effectiveness of dust dispersion in the 20 L Siwek chamber, *Journal of Loss Prevention in the Process Industries* 23 (1) (2010) 46–59.

- [4] B. Du, W. Huang, L. Liu, T. Zhang, H. Li, Y. Ren, H. Wang, Visualization and analysis of dispersion process of combustible dust in a transparent Siwek 20-l chamber, *Journal of Loss Prevention in the Process Industries* 33 (2015) 213–221.
- [5] A. Di Benedetto, P. Russo, R. Sanchirico, V. Di Sarli, Cfd simulations of turbulent fluid flow and dust dispersion in the 20 L explosion vessel, *AIChE Journal* 59 (7) (2013) 2485–2496.
- [6] W. Pollhammer, C. Spijker, H. Kern, H. Raupenstrauch, Development of a dust dispersion system for investigations on reduced pressure conditions in the 20 L Siwek apparatus using OpenFOAM, 2015.
- [7] W. Jones, R. Lindstedt, Global reaction schemes for hydrocarbon combustion, *Combustion and Flame* 73 (3) (1988) 233–249.
- [8] A. Islas, A. R. Fernández, C. Betegón, E. Martínez-Pañeda, A. Pandal, Computational assessment of biomass dust explosions in the 20 L sphere, *Process Safety and Environmental Protection* 165 (2022) 791–814.
- [9] T. Poinso, D. Veynante, *Theoretical and Numerical Combustion*, RT Edwards, Inc., 2005.
- [10] J. Powers, *Combustion Thermodynamics and Dynamics*, Cambridge University Press, Cambridge, UK, 2016.
- [11] J. Chomiak, *Combustion: A Study in Theory, Fact, and Application*, Abacus Press, Philadelphia, PA, USA, 1990.
- [12] M. A. Liberman, Effects of radiation on particle-laden combustion, in: *Combustion Physics: Flames, Detonations, Explosions, Astrophysical Combustion, and Inertial Confinement Fusion*, Springer International Publishing, 2021, pp. 465–496.
- [13] M. F. Modest, *Radiative Heat Transfer*, 3rd Edition, Elsevier, 2013.
- [14] W. E. Ranz, W. R. Marshall, Evaporation from drops, *Chemical Engineering Progress* 48 (1952) 141–146, 173–180.
- [15] W. Cao, Q. Qin, W. Cao, Y. Lan, T. Chen, S. Xu, X. Cao, Experimental and numerical studies on the explosion severities of coal dust/air mixtures in a 20 L spherical vessel, *Powder Technology* 310 (04 2017).
- [16] M. M. Baum, P. J. Street, Predicting the combustion behavior of coal particles, *Combustion Science and Technology* 3 (5) (1971) 231–243.
- [17] R. K. Boyd, J. H. Kent, Three-dimensional furnace computer modeling, in: *21st Symposium (International) on Combustion*, The Combustion Institute, 1986, pp. 265–274.
- [18] A. Putnam, Integratable form of droplet drag coefficient, *ARS Journal* 31 (10) (1961) 1467–1468.
- [19] A. A. Amsden, P. J. O'Rourke, T. D. Butler, Kiva-II: A computer program for chemically reactive flows with sprays, Tech. Rep. LA-11560-MS, Los Alamos National Lab. (LANL), Los Alamos, NM (United States) (1989).
- [20] R. B. Bird, W. E. Stewart, E. N. Lightfoot, *Transport Phenomena*, 2nd Edition, John Wiley & Sons, New York, 2002.
- [21] S. H. Spitzer, A. Pandal, M. V. Rodríguez, M. Schmidt, E. Danzi, O. Dufaud, B. Janovsky, Investigations on different distribution systems for dusts inside the 20l-sphere, *Journal of Loss Prevention in the Process Industries* 92 (2024) 105492.
- [22] H. Rasam, M. Nematollahi, S. Sadeghi, M. Bidabadi, An asymptotic assessment of non-premixed flames fed with porous biomass particles in counter-flow configuration considering the effects of thermal radiation and thermophoresis, *Fuel* 239 (2019) 747–763.
- [23] M. Portarapillo, R. Sanchirico, G. Luciani, A. Di Benedetto, Flame propagation of combustible dust: A Mallard-Le Chatelier inspired model, *Combustion and Flame* 251 (2023) 112737.
- [24] Y. Pan, Flame behavior of coal dust explosion considering internal particle effects, Ph.D. thesis, Montanuniversitaet Leoben (2023).
- [25] C. R. L. Bauwens, L. R. Boeck, S. B. Dorofeev, Understanding the limitations of using k_{st} to define the reactivity of large scale dust explosion tests, in: *Proceedings of the 15th International Symposium on Hazards, Prevention, and Mitigation of Industrial Explosions*, Naples, Italy, 2024, pp. 21–32.